

Large Scale Two-Dimensional Flux-Closure Domain Arrays in Oxide Multilayers and Their Controlled Growth

Ying Liu,[†] Yu-Jia Wang,[†] Yin-Lian Zhu,^{*,†,‡,§} Chi-Hou Lei,[‡] Yun-Long Tang,[†] Shuang Li,[†] Si-Rui Zhang,[†] Jianguy Li,^{§,||} and Xiu-Liang Ma^{*,†,⊥}

[†]Shenyang National Laboratory for Materials Science, Institute of Metal Research, Chinese Academy of Sciences, Wenhua Road 72, 110016 Shenyang, China

[‡]Department of Aerospace and Mechanical Engineering, Saint Louis University, Saint Louis, Missouri 63103-1110, United States

[§]Shenzhen Key Laboratory of Nanobiomechanics, Shenzhen Institutes of Advanced Technology, Chinese Academy of Sciences, University Town of Shenzhen, Shenzhen, Guangdong 518055, China

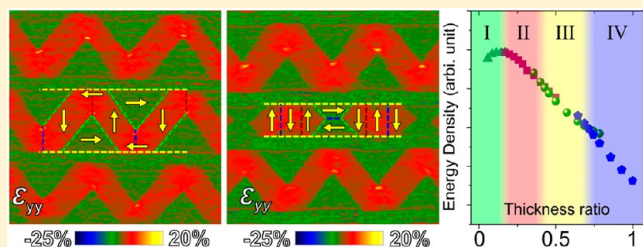
^{||}Department of Mechanical Engineering, University of Washington, Seattle, Washington 98195-2600, United States

[⊥]School of Materials Science and Engineering, Lanzhou University of Technology, 730050 Lanzhou, China

Supporting Information

ABSTRACT: Ferroelectric flux-closures are very promising in high-density storage and other nanoscale electronic devices. To make the data bits addressable, the nanoscale flux-closures are required to be periodic via a controlled growth. Although flux-closure quadrant arrays with 180° domain walls perpendicular to the interfaces (V-closure) have been observed in strained ferroelectric PbTiO₃ films, the flux-closure quadrants therein are rather asymmetric. In this work, we report not only a periodic array of the symmetric flux-closure quadrants with 180° domain walls parallel to the interfaces (H-closure) but also a large scale alternative stacking of the V- and H-closure arrays in PbTiO₃/SrTiO₃ multilayers. On the basis of a combination of aberration-corrected scanning transmission electron microscopic imaging and phase field modeling, we establish the phase diagram in the layer-by-layer two-dimensional arrays versus the thickness ratio of adjacent PbTiO₃ films, in which energy competitions play dominant roles. The manipulation of these flux-closures may stimulate the design and development of novel nanoscale ferroelectric devices with exotic properties.

KEYWORDS: Ferroelectric oxide, PbTiO₃, flux-closure domain, aberration corrected scanning transmission electron microscope, phase field modeling



Topological defects such as vortices in superconductors/superfluids/ferroics, domain walls in ferroics, and dislocations/disclinations in crystalline/liquid crystals have attracted great attention due to their nontrivial mechanical, electronic, magnetic behaviors and potential applications in nanoscale device engineering.^{1–7} A ferroelectric vortex state is a kind of exotic topological state generally discussed in low dimensional ferroelectric materials. This state could possess peculiar properties, for example, an enhanced electronic conductivity at vortex cores as revealed in BiFeO₃ thin films.³ They have become a subject of intensive interest^{8–22} since the initial predictions in BaTiO₃ and PbZr_xTi_{1-x}O₃ nanostructures about ten years ago.^{23,24} Using piezoelectric force microscopy, “closed” domain patterns have been frequently observed in ferroelectrics such as BaTiO₃ single crystals or nanodots, BiFeO₃ and PbZr_xTi_{1-x}O₃ thin films, though they are often composed of shape-conserved ferroelastic domains.^{12–14,25} Employing aberration corrected (scanning) transmission electron microscope ((S)TEM),^{26,27} continuous dipole rotations, flux-closure quadrants, and symmetrical 4-fold flux-

closure domains were successfully observed in ferroelectric thin films.^{28–32}

Ferroelectric flux-closures, which exhibit closed head-to-tail continuous electric dipoles, are very promising in high density storage, because data storage in these domain patterns may avoid the problem of “cross-talk”. In order for the data bits to be addressable, nanoscale flux-closures should be periodic. Recently, some efforts have been devoted to obtaining periodic flux-closure or vortex domain arrays, which shed light on the self-assembly of electronic devices at nanoscale.^{30,32–34} In 2015, by incorporating a thin layer of SrTiO₃ (STO) to produce an insulated boundary condition on ferroelectric PbTiO₃ (PTO) thin films grown on GdScO₃ (GSO) substrates, Tang et al. successfully observed periodic vertical flux-closure domain arrays with 180° domain walls perpendicular to the interface.³⁰ Subsequently, Yadav et al. deposited PTO/STO superlattices on DyScO₃ (DSO) substrates and obtained vortex arrays which

Received: June 21, 2017

Revised: November 9, 2017

Published: November 10, 2017

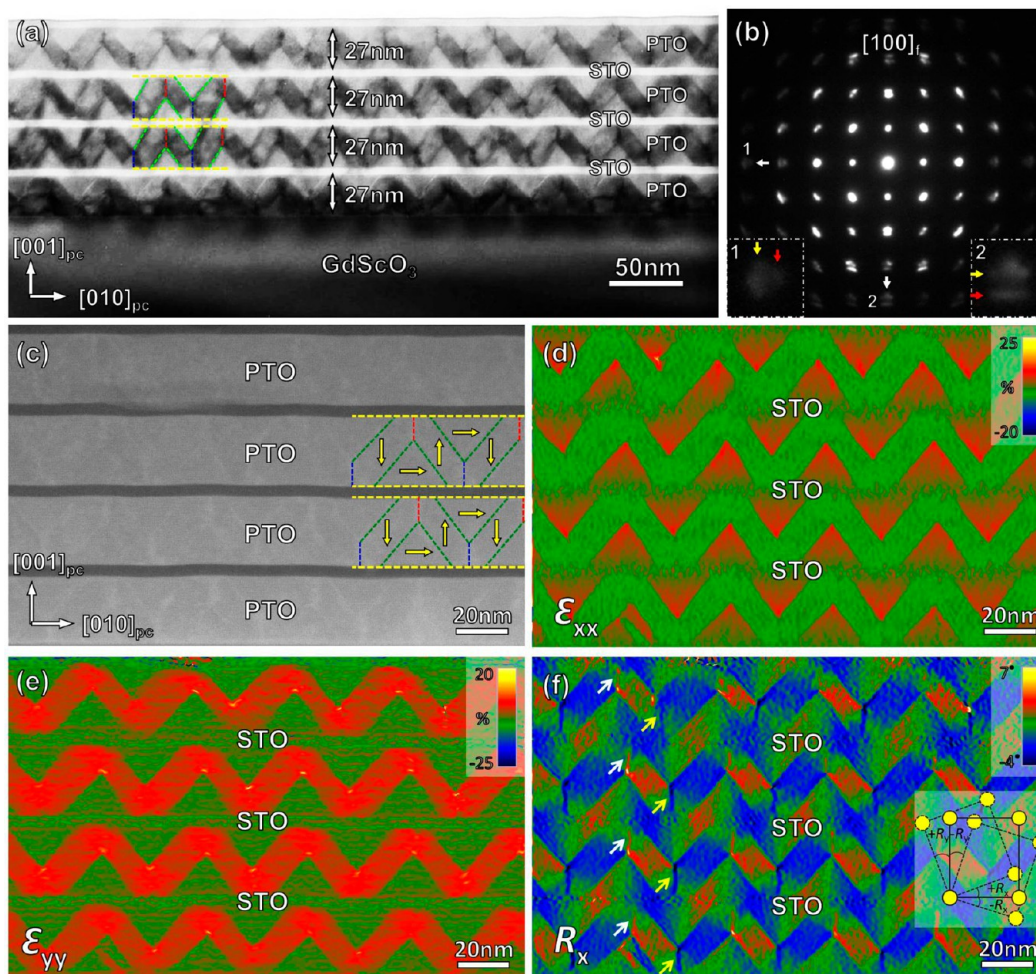


Figure 1. Identification of 2D neatly arranged vertical flux-closure quadrants in the $(\text{PTO}(27 \text{ nm})/\text{STO}(4 \text{ nm}))_4$ multilayered film grown on the $\text{GSO}(001)_{\text{pc}}$ substrate. The thickness ratio of adjacent PTO layers is 1. (a) A TEM BF image of the PTO/STO multilayered film showing periodic flux-closure quadrants in both horizontal and vertical directions. (b) An electron diffraction pattern taken from the PTO/STO film. Diffraction spots “1” and “2” are enlarged and shown in the corresponding insets. Yellow and red arrows indicate the diffusing diffraction spots of c - and a -domains, respectively. (c) The HAADF-STEM image of the film with the polarization directions (yellow arrows) determined by the lattice rotation analysis (f). (d–f) GPA analysis of the in-plane lattice strain (d), out-of-plane lattice strain (e) and in-plane lattice rotation (f) of (c). In (a,c), yellow and green dashed lines are used to mark PTO/STO interfaces and 90° domain walls, respectively; red and navy blue dashed lines represent 180° domain walls; yellow arrows show the polarization directions.

show periodicity in two dimensions (2D).³² However, in the out-of-plane direction, the periodicity is relatively undefined: the locations of vortices of the same chirality seem random in this direction. The formation of ferroelectric domain structures is the result of the competition of several energies. In the paper of Yadav et al.,³² phase field simulations were performed to compare the total energies of three different domain structures: a_1/a_2 , vortex, and flux-closure, successfully explaining the formation condition of vortex array, from the perspective of energy competition. In this work, we took into account the giant disclination strain characteristics of flux closure domain pattern and the fact that the horizontal period of the flux closures is $\sqrt{2}$ times of PTO thickness,³⁰ and grew PTO/STO multilayer films on $\text{GSO}(001)_{\text{pc}}$ substrates with multiple periodicities. By controlling the thickness ratio of adjacent PTO layers, we obtained a 2D distribution of vertical flux-closure domain arrays (named V domains) in PTO layers of equal thickness; furthermore, both vertical and horizontal arranged flux-closure domain arrays (named H domains) with periodic distribution were observed in adjacent PTO layers when

varying their thickness ratio. These experimental results are consistent with the phase diagram of domain pattern versus PTO thickness ratio established by our phase field simulations. These experimental findings and theoretical understanding will provide valuable information for the development of novel nanoscale ferroelectric devices.

PTO is a tetragonal ferroelectric with the lattice parameters of $a = b = 3.90 \text{ \AA}$ and $c = 4.15 \text{ \AA}$.³⁵ The schematic of the PTO crystal structure is shown in Figure S1. Because of the strong coupling between ferroelectricity and tetragonality in this classic ferroelectric,³⁶ a PTO layer containing periodical flux-closure array displays a giant disclination strain, which exerts a periodical out-of-plane strain state for the film grown on it.^{30,37} This unique strain state may facilitate a regularly arranged microstructure. First of all, when a $(\text{PTO}/\text{STO})_n$ multilayered structure is fabricated in which all the PTO layers share the same thickness, each PTO layer may adopt the previous layer's strain, making all the PTO layers feature the same flux closure domain period. This is verified by the experiment result shown in Figure 1. The thickness of PTO (27 nm) was selected within

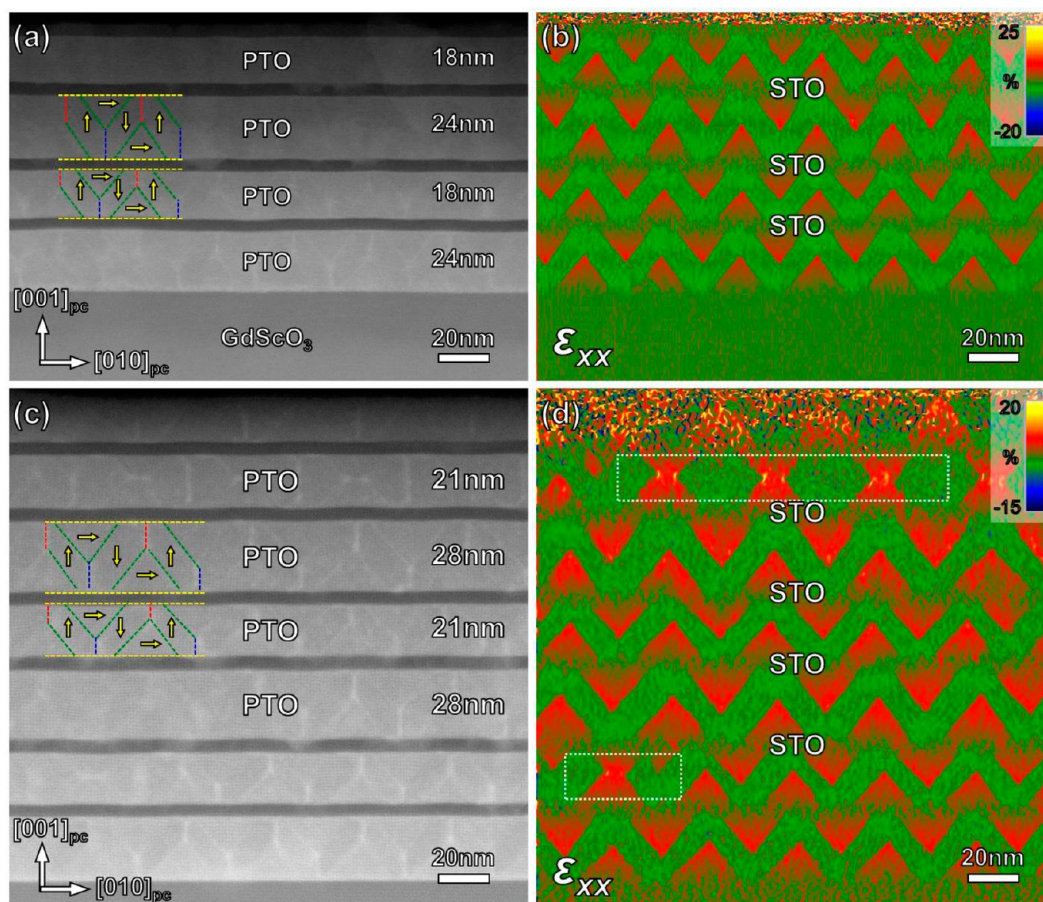


Figure 2. Domain configurations in two multilayered PTO/STO films grown on GSO (001)_{pc} substrates with the thickness ratio of 0.75 in adjacent PTO layers. (a) An HAADF-STEM image of the PTO(24 nm)/STO(4 nm)/PTO(18 nm)/STO(4 nm)₂ film and (b) the corresponding in-plane strain map obtained from GPA. Vertical flux-closure domains can be observed. (c) An HAADF-STEM image of (PTO(28 nm)/STO(5 nm)/PTO(21 nm)/STO(5 nm))₄ multilayers and (d) the corresponding in-plane strain map obtained from GPA. Besides vertically arranged flux-closure domains, horizontal domains can be seen as outlined by dotted rectangles. The color scheme is the same as that in Figure 1.

the range of flux-closure formation as proposed by Tang et al.,³⁰ and the thickness of STO layers (4 nm) was selected, which is thin enough to make sure that the out-of-plane strain generated by flux-closure domain arrays in the underneath layer could be transferred into the above PTO layer.

Figure 1a is a bright-field (BF) TEM image showing the morphology of the (PTO(27 nm)/STO(4 nm))₄ film grown on the GSO (001)_{pc} substrate, where the subscript “4” denotes four layers of PTO/STO unit. In this image, STO layers show bright contrast while PTO layers adopt a periodic “V”- and “Λ”-shaped contrast. This morphology characteristic is similar to the alternate clockwise and counterclockwise flux-closure quadrants in multilayer PTO/STO films reported previously.³⁰ Surprisingly, these flux-closures quadrants not only arrange periodically in one single PTO layer along the horizontal direction but also in different PTO layers along the vertical direction, that is, forming a 2D pattern. A selected area electron diffraction of the film is shown in Figure 1b. The diffraction spots indicated by white arrows and labeled by “1” and “2” are enlarged and shown in the corresponding insets. Diffraction spots of *a*-domains (red arrows) can be differentiated from those of *c*-domains (yellow arrows), because *a*-domains have larger in-plane and smaller out-of-plane lattice parameters. Both *a*- and *c*-domain diffraction spots are diffusional due to the nonuniform strain of flux closure quadrants. To further verify

the flux-closure domain pattern, HAADF-STEM imaging of the PTO/STO multilayer and corresponding geometric phase analysis (GPA)^{38–40} of lattice strains and lattice rotation were conducted and shown in Figure 1c–f. In the PTO layer, some bright lines can be traced, as shown in Figure 1c, which are supposed to be induced by the domain walls of four quadrants closure domains as the case in ref 30. To clearly reveal the domains, in-plane and out-of-plane strain maps are shown in Figure 1d,e, respectively. The *a*-domains are in red and *c*-domains are in green in Figure 1d, while their colors are the opposite in Figure 1e. Figure 1f shows the corresponding in-plane lattice rotation map (R_x). It is noted that 180° domain walls are revealed as short red and blue lines, as indicated by white and yellow arrows, which represent a positive and a negative in-plane lattice rotation (the in-plane and out-of-plane (R_y) lattice rotations are defined in the inset of Figure 1f).^{30,41–44} These red lines suggest that the polarizations point downward on the left of a 180° domain wall and upward on the right, and the case of blue lines is opposite.^{42–45} According to the polarization directions around 180° domain walls (shown as yellow arrows in Figure 1c), we can confirm the alternate clockwise and counterclockwise flux-closure quadrants. Besides the (PTO(27 nm)/STO(4 nm))₄ film, a (PTO(27 nm)/STO(4 nm))₈ film with eight PTO layers was also grown on the GSO (001)_{pc} substrate, as shown in the Supporting

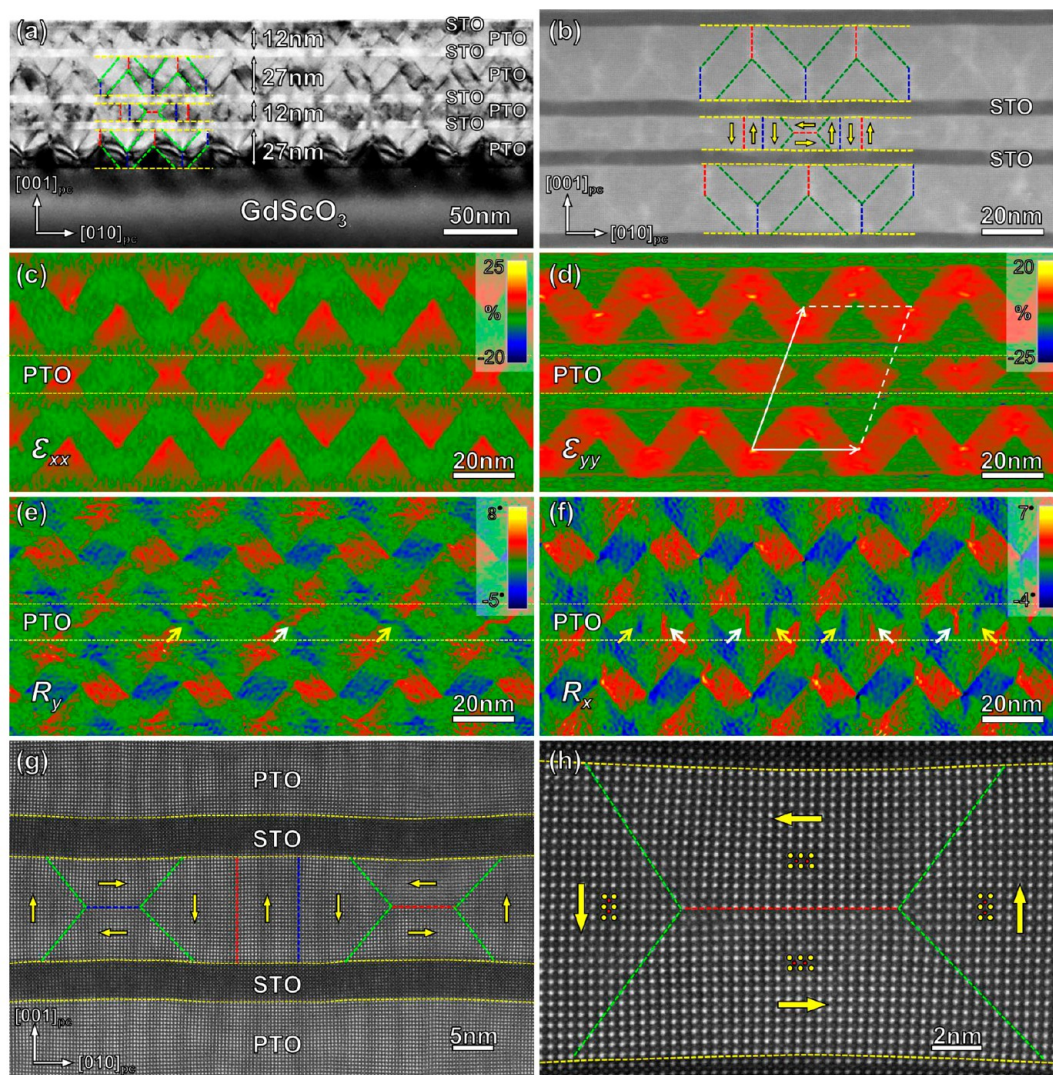


Figure 3. Identification of 2D regularly arranged vertical and horizontal flux-closure quadrants in the (PTO(27 nm)/STO(4 nm)/PTO(12 nm)/STO(4 nm))₂ multilayered film grown on the GSO(001)_{pc} substrate. The thickness ratio of adjacent PTO layers is about 0.5. (a) A TEM image of the PTO/STO multilayer film showing that periodic vertical flux-closure quadrants form in the 27 nm thick PTO layers, while horizontal flux-closure quadrants periodically arrange in the 12 nm thick PTO layers. (b) An HAADF-STEM image of the film. (c, d) In-plane and out-of-plane lattice strain maps of (b). (e, f) Out-of-plane and in-plane lattice rotation maps of (b). White and yellow arrows in (f) denote 180° domain walls with positive and negative lattice rotations, respectively. (g, h) Enlarged HAADF-STEM images showing domain structures in a 12 nm PTO layer. Yellow arrows in (g, h) mark P_s directions. In (a, b, g, h), dashed lines and arrows are used to mark interfaces, domain walls, and polarization directions. The color scheme is the same as that in Figure 1.

Information (Figure S2), and the same regularly arranged flux-closure domain patterns were observed. These experimental results indicate that due to the giant disclination strain induced by closure domains, as we show in details later, the 2D periodicity of vertical flux-closure arrays is still present in PTO/STO multilayer films with very large thicknesses.

The horizontal period (w) of the flux-closure array in our (PTO(27 nm)/STO(4 nm))₄ multilayer film grown on the GSO(001)_{pc} substrate were estimated to be 38 nm, which is about $\sqrt{2}$ times of the PTO thickness d (about 27 nm). This relationship between d and w is consistent with that reported previously.³⁰ In the vertical direction, flux-closure quadrants also arranged regularly. The main driving force for the formation of this arranged domain pattern is supposed to be the elastic energy: in the horizontal direction, the tensile strain provided by the substrate facilitates the formation of flux closure domains, while the accommodation of the strain states

of the flux closure domains in adjacent PTO layers results in the periodicity in the vertical direction. Of course, the primary condition is that all PTO layers are at the same thickness, so that the flux-closure arrays could adopt the same period according to the relationship between the flux closure domain period and the PTO thickness.³⁰ In the following, we show some other multilayer films in which adjacent PTO layers adopt different thicknesses.

Figure 2 shows the domain patterns of PTO/STO multilayer films with adjacent PTO layers adopting a thickness ratio of 3/4. Figure 2a is an HAADF-STEM image of PTO/STO multilayers, in which four PTO and STO layers were grown alternatively and the thicknesses of adjacent PTO layers are 24 and 18 nm, respectively. The corresponding GPA of in-plane lattice strain (ϵ_{xx}) is shown in Figure 2b, where a -domains are in red and c -domains are in green. From this strain map, a wavy (green) characteristic in every PTO layer, which is similar to

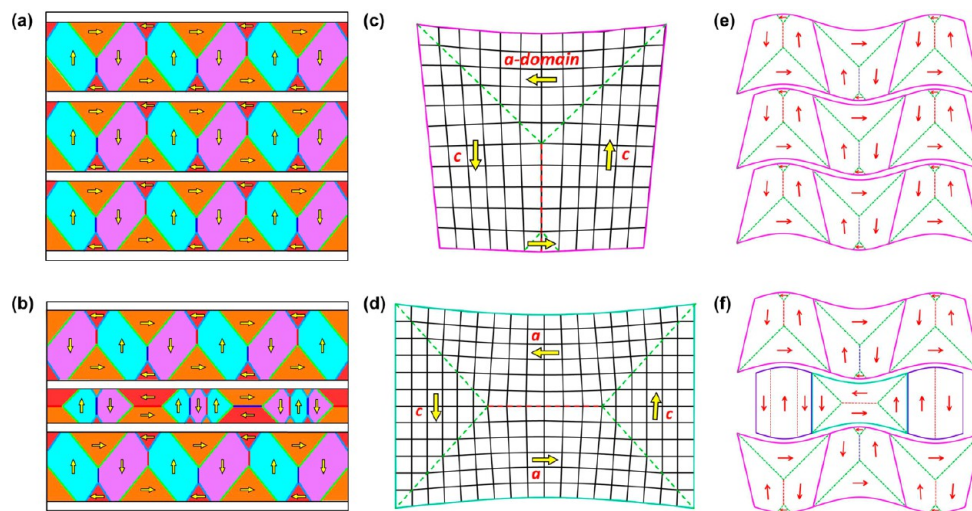


Figure 4. Schematics and strain analyses of flux-closure domain patterns in PTO/STO multilayers. (a) Two dimensional distributions of V domains in PTO layers when the thickness ratio of adjacent PTO layers is 1. (b) Besides V domains, H domains were found in thin PTO layers when the thickness ratio of adjacent PTO layers is about 0.5. Yellow arrows indicate P_s directions. Navy blue and red lines denote 180° domain walls. Green and light blue lines indicate 90° domain walls. (c,d) Schematics of lattice strain in vertical (c) and horizontal (d) flux-closure domain patterns, where black grids denote PTO lattices. (e) A schematic shows that when the thickness of each PTO layer is the same, the formation of the neatly arranged vertical flux-closure quadrants could prefer to accommodate the strain in each layer properly. (f) A schematic shows the case that the difference of thicknesses of adjacent PTO layers is relatively large. In thick PTO layers, vertical flux-closure quadrants are periodically arranged, and the flux-closure arrays in adjacent thick PTO layers have a phase shift of one-half period, whereas in the thin PTO layers, horizontal flux-closure quadrants form to mediate the disclination strain of the two thick PTO layers. Arrows indicate P_s directions.

that in Figure 1e, is revealed, suggesting a periodic clockwise and counterclockwise vertical flux-closure domain pattern. A PTO/STO multilayer film with eight PTO and STO layers was also grown. The HAADF-STEM image and corresponding in-plane strain map (ϵ_{xx}) in Figures 2c and 2d prove that this domain pattern preserves to more layers though some “funnel”-shaped a -domains (marked by white dotted boxes) are occasionally present, which will be analyzed in detail in the next paragraph. Although the thicknesses of adjacent PTO layers are different, their horizontal periods (w) are the same (see the strain maps in Figures 2b and 2d). In Figure 2a and 2b, the horizontal period of the flux-closure arrays is estimated to be about 30 nm, which is close to the average of the intrinsic periods of the two PTO layers (the intrinsic periods of thick and thin PTO layers are 33.9 and 25.5 nm, as determined by $w = \sqrt{2d}$).³⁰ This is suggested to be the result of a competition between the two periods or strain states in the two PTO layers. In Figures 2c and 2d, the horizontal period of the flux-closure array is estimated to be about 41 nm, which is close to and even somewhat larger than the intrinsic period of the thick PTO layers (39.6 nm). The phenomenon shows that the formation of “funnel”-shaped a -domains in the thin PTO layers helps relax the strain, making the flux-closure arrays in the thick PTO layers adopt their intrinsic period.

Then, we further enlarged the thickness difference between adjacent PTO layers to let the thickness ratio be 1/2. Figure 3a is a TEM BF image of the (PTO(27 nm)/STO(4 nm)/PTO(12 nm)/STO(4 nm))₂ film. In the 27 nm PTO layers, periodic “V”- and “Λ”-shaped domains, similar to those in Figure 1a, are observed, which is a typical characteristic of the alternate clockwise and counterclockwise flux-closure quadrants. However, the flux-closure arrays in the adjacent 27 nm PTO layers show a phase shift of one-half period. A different domain pattern appears in the 12 nm PTO layer which is sandwiched by two 27 nm ones. In the HAADF-STEM image

of the multilayer film shown in Figure 3b, a few bright line contrasts, which correspond to 90° and 180° domain walls, can be identified. Figure 3c,d shows in-plane and out-of-plane lattice strain maps of Figure 3b. From these strain maps, a - and c -domains in the 12 nm PTO layer can be determined, where a -domains look like “funnels”, and other areas are c -domains. A periodic a - and c -domain pattern can be revealed, whose period is equal to that of vertical flux-closure arrays in 27 nm PTO layers ($w = 38$ nm), and the relationship between thickness and period accords with the scaling law $w = \sqrt{2d}$ in the thick (27 nm) PTO layer.³⁰ To further analyze the domain pattern, in-plane and out-of-plane lattice rotation were analyzed. Figure 3e,f shows the out-of-plane and in-plane lattice rotation maps. In the a -domain area of the 12 nm PTO layer, horizontal 180° domain walls can be identified (red and blue lines as indicated by white and yellow arrows, Figure 3e), while vertical 180° domain walls can be revealed in the c -domain areas (denoted also by arrows, Figure 3f). According to the lattice rotation values of these 180° domain walls, P_s directions can be determined in each area (Figure 3b). Enlarged HAADF-STEM images shown in Figure 3g,h give direct evidence of the PTO/STO interface configuration and polarization directions in the thin PTO layer. In Figure 3g, obvious wavy PTO/STO interfaces are observed, which is an indication of the giant disclination strain. In Figure 3h, the domain pattern with closed head-to-tail dipole moments are determined by reversed Ti displacement vectors with respect to their nearest Pb.^{30,45,46} We can clearly see that a “funnel” and two nearby c -domains form a symmetric 4-fold flux-closure quadrant.³¹ Because the 180° domain walls lie horizontally, we label this kind of flux-closure quadrants in terms of H domains in order to differentiate them from the V domains in the 27 nm PTO layers, where the 180° domain walls are vertically oriented. The PTO/STO interfaces are found to be bent due to the large disclination strain.

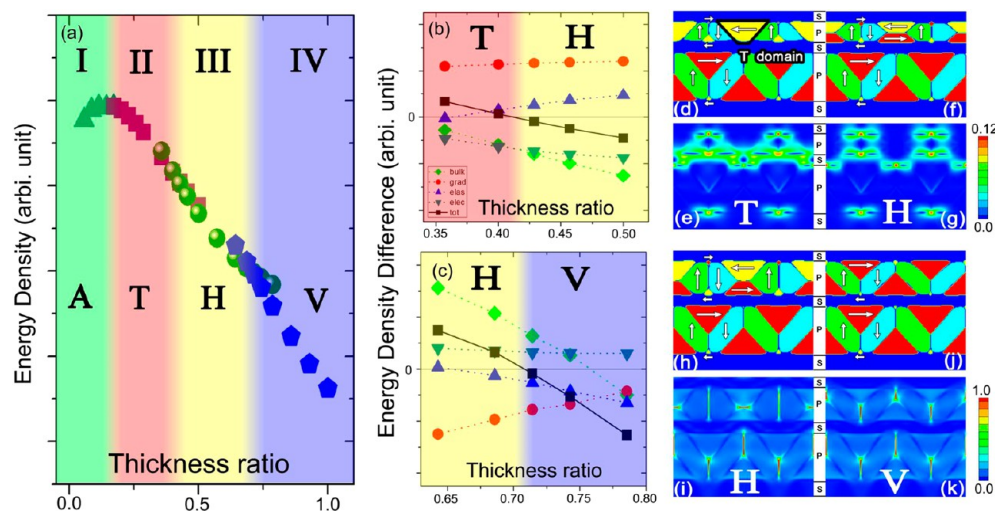


Figure 5. Phase diagram of the flux-closure domains as a result of energy minimization. (a) Total energy density in the multilayered PTO/STO systems as the function of the thickness ratio. Four regions (I, II, III, and IV) can be found in which a_1 and a_2 domains (A), trapezoid a -domains (T), horizontal flux-closures domains (H) and vertical flux-closure domains (V) are dominant, respectively. (b) Energy density differences of H domains and T domains near the second transition. (c) Energy density differences of V domains and H domains near the third transition. (d–g) The domain structure and electrostatic energy density maps for T domains (d,e) and H domains (f,g), respectively. One T domain is separated by two 90° domain walls and occupies the whole PTO film in the vertical direction, as marked by a black trapezoid in (d). (h–k) The domain structures and elastic energy density maps for H domains (h,i) and V domains (j,k), respectively. The thickness ratios in (d–g) and (h–k) are 0.43 and 0.71, respectively, close to the two transition points.

In Figure 3, we can see that a combination of thick and thin PTO layers shows some extent of periodicity in the vertical direction. We further verify this tendency by growing a PTO/STO film with a thickness ratio of one-half and having more layers. The corresponding results are shown in Figures S3 and S4. Figure S3 is a TEM BF image of a (PTO(27 nm)/STO(4 nm)/PTO(12 nm)/STO(4 nm))₄ multilayer film, showing a large area of domain morphology. In this image, a regularly arranged domain pattern can be identified. V domains are observed in the thick PTO layer while the domain pattern in the thin PTO layer is not very clear. A further HAADF-STEM image (Figure S4a) was taken and the corresponding out-of-plane lattice strain mapping was conducted (Figure S4b). From Figure S4b, we can clearly see that H-domains lie in the thin PTO layer. If we consider one horizontal quadrant and two vertical ones in adjacent PTO layers as a unit, a 2D periodicity for this unit is formed and described by a parallelogram (this unit is also plotted in Figure 3d). One basis vector is along the horizontal direction and the other one is at an angle to the vertical direction as denoted by arrows. As a result, the V and H domains display periodicity in two dimensions.

Figure 4a,b shows schematic illustrations of the 2D distribution of two types of flux-closure domains (corresponding to Figures 1 and 3). For the films in which all the PTO layers share identical thicknesses (Figure 4a), the 2D periodicity of the flux closures is obvious. The films with thickness ratio of about one-half (Figure 4b), the presence of domains is also in a regular manner, especially in the thick PTO layer. In the thin PTO layer, the 2D periodicity can be found in the strain map (Figure 3b), and the H domains (see the middle layer in Figure 4b) only show weak periodicity, since the curls of these flux-closures seem to be random.

It is known that strains in oxide thin films play significant roles in determining the microstructures and associated physical properties.^{47,48} However, previous literatures usually focused on the in-plane biaxial strain provided by substrates,⁴⁸ while the strain along out-of-plane direction was scarcely discussed. In

this work, we found that both in-plane and out-of-plane strains play important roles in the formation of such highly ordered domain patterns, from the perspective of the strain accommodation. Figure 4c,d schematically shows the lattice characteristics of a V domain and an H domain. The PTO layer containing V domains becomes wavy due to the periodic disclination strain. When PTO layers with identical thickness are deposited layer-by-layer, the most natural packing style is the one shown in Figure 4e where the periodic array of the closures appears in the same way for all the PTO layers. This is because the closure domains and the resultant strains in each PTO layer have the same intrinsic period, and any horizontal shift between PTO layers must result in large elastic energy. Therefore, the V domains tend to arrange periodically not only in a single PTO layer but also along the out-of-plane direction of the multilayers, forming a 2D periodic closure domains pattern. If adjacent PTO layers adopt different thicknesses and the difference is relatively small (e.g., the adjacent PTO thickness ratio is three-quarters), V domains could also form in adjacent PTO layers. Since their intrinsic periods slightly differ from each other, the two periods may interact to form an averaged one, which is the case shown in Figure 2a,b. However, when the thickness of the PTO/STO multilayer is increased from 4 to 8 layers, not only V domains but also some H domains are created (Figure 2c,d). We propose that it would be more difficult to modulate the strain and reach an equilibrium state in PTO/STO with more layers. Furthermore, the emergence of a local H domain may suggest that this kind of domain also contributes to the accommodation of the strain when adjacent PTO layers adopt different thicknesses as stated above. If the thickness difference of adjacent PTO layers is relatively large (adjacent PTO thickness ratio is one-half), the two intrinsic periods cannot be well matched by the formation of V domains only, instead, a different domain pattern, like H domains, is introduced in the thin PTO layer to appropriately mediate this strain. From Figure 4f, we see that when a relative shift of one-half period between the two wavy thick PTO layers

is present, the introduction of H domains can match the shape of the two wavy layers perfectly.

To gain a deeper understanding of the formation of different domain structures, we performed phase-field simulations to systematically study the evolution of domain structures relative to the variance of PTO thickness ratio. The model contains two PTO and three STO layers that are alternatively arranged. To keep pace with experimental results, the lower PTO layer was set as 28 nm thick and filled with V domains. We systematically changed the thickness of the upper PTO layer from 0 to 28 nm. Figure 5a shows the variance of the total energy density as a function of the thickness ratio. Depending on the energy density distribution, four regions were outlined as marked by "I", "II", "III", and "IV", in which four kinds of domains are dominant, when the thickness ratio changes from 0 to 1. In the region "I", the polarizations in the upper PTO layer mainly lie along [100] and [010] directions, as shown in Figure 5Sa. The ferroelectric domains with [100] or [010] polarizations are commonly marked as *a*-domains, so that this region is named as "A". In the second region, trapezoidal (where the symbol "T" comes from) *a*-domains, separated by 90° domain walls from vortices, are the most stable domain structure in the upper PTO layer, as marked in Figure 5d. The domain structures in the two regions are predicted by phase field simulations. In the third region, H domains are favorable in the upper PTO layer, as shown in Figure 5f and 5Sd. In the fourth region, V domains are the most stable in the upper PTO layer, whose period is exactly the same as the ones in the lower PTO layer, as shown in Figure 5j and 5Sf. H and V domains in the regions "III" and "IV" are experimentally observed, as shown in Figures 3 and 1, respectively.

Actually, at a thickness ratio of about 0.1–0.2, the division between the regions "I" and "II" is not very clear. In contrast, the other two transition points (0.4 and 0.7) can be accurately determined by spotting the positions at which the total energy density difference (ΔE_{tot} blocks) between two domain structures is zero, as shown in Figure 5b,c. The thickness ratios in Figures 1 and 3 are about 1.0 and 0.5, which pertains to the regions of "V" and "H". Indeed, V and H domains were observed in these two samples, respectively. In the case with the thickness ratio of 0.75 shown in Figure 2, which approaches the transition point between V and H domains, both V and H domains can be found in Figure 2. This indicates that the competition of these two different domain structures occurs near the phase transition point. The phase diagram of the domain structure vs the PTO thickness ratio established by the phase field simulations is perfectly consistent with our experimental results. In the following, we further analyze the driving forces for the transitions between different domain structures.

At the transition from T to H, the driving forces are the bulk (diamonds) and electrostatic (downward triangles) energies since ΔE_{bulk} and ΔE_{elec} are negative (Figure 5b), while the gradient (round dots) and elastic (upward triangles) ones hinder the transition for ΔE_{grad} and ΔE_{elas} are positive (Figure 5b). At the transition from H to V, the case is just opposite (Figure 5c): the gradient and elastic energies overwhelm the bulk and electrostatic ones at the transition point. To further validate the tendency, we select and cope with two transition points: one is between T and H domains, and the other is between H and V domains. Figure 5d–g exhibits the domain structures and electrostatic energy distributions of T and H domains in the multilayer systems with the thickness ratio of

0.43 (close to the first transition point). When the transition occurs, the area of the interfaces between *c*-domains in the upper PTO layer and the middle STO layer reduces, resulting in the reduction of the depolarization field. As a result, the electrostatic energy gets reduced. The bulk energy minimum is reached when the polarization magnitude in every place adopts the spontaneous one. In T domains, the stronger depolarization field depresses the polarization, so that the bulk energy also increases. As a result, H domains are stabilized. Figure 5h–k displays the domain structures and elastic energy distributions of H and V domains in the multilayer systems with the thickness ratio of 0.71 (close to the second transition point). The elastic energy is largely localized at the 180° domain walls. As the transition happens, the amount of 180° domain walls reduces, so does the elastic energy. The gradient energy also concentrates at the 180° domain walls where the polarization gradient is the largest, thus playing the same role as the elastic energy. As a result, V domains are favorable. In addition, it is worthwhile to point out that if the thickness ratio is below 0.4, the domains may evolve into vortex-like patterns in thin PTO layers, just like the case in ref 32.

In summary, we have designed and grown periodic arrays of the ferroelectric flux-closure quadrants in PTO/STO multilayers. By tuning the thickness ratio of adjacent PTO layers we have obtained two configurations of the flux-closure array: one with 180° domain walls perpendicular to the interfaces (V-closure) and another with 180° domain walls parallel to the interfaces (H-closure). When the PTO thickness is fixed in the multilayer (thickness ratio of adjacent PTO layers is 1), a periodic V-type flux-closure array is observed in each PTO layer. When the thickness ratio of adjacent PTO layers ranges at 0.4–0.7, a periodic V-type flux-closure array is identified in the thicker PTO layer and a horizontal flux-closure array is found in the thinner PTO layer. A phase diagram of flux-closure domains versus thickness ratio of adjacent PTO layers is established by phase field simulations and confirmed by aberration corrected scanning transmission electron microscopic observation. The controlled growth of the 2D flux-closure domain array makes a great step toward the realization of ferroelectric nanoscale devices.

METHODS

Film Deposition Details. (PTO(27 nm)/STO(4 nm))₄, (PTO(27 nm)/STO(4 nm))₈, (PTO(27 nm)/STO(4 nm)/PTO(12 nm)/STO(4 nm))₂, and (PTO(27 nm)/STO(4 nm)/PTO(12 nm)/STO(4 nm))₄ multilayered films were deposited on GSO (001)_{pc} substrates by pulsed laser deposition, using a Coherent CompExPRO 201FKrF ($\lambda = 248$ nm) excimer laser. Before deposition, the substrate was heated to 800 °C for 10 min to clean the substrate surface and then cooled down to the film deposition temperature. When growing both PTO and STO, a repetition rate of 4 Hz, substrate temperature of 700 °C, and oxygen pressure of 75 mTorr were used. During the growth of PTO, a 3 mol % Pb-enriched sintered ceramic target and laser energy of 350 mJ were used, while a stoichiometric target and a laser energy of 250 mJ were used when growing STO. After growth, the film was annealed at 700 °C in an oxygen pressure of 0.5 atm for 10 min and then cooled to room temperature slowly at a rate of 5 °C/min.

TEM Sample Preparation, (S)TEM Observation, and Geometry Phase Analysis (GPA). The samples for the TEM and STEM observation were prepared by slicing, grinding, dimpling, and finally ion milling. TEM and HAADF-STEM

images were recorded using aberration-corrected (scanning) transmission electron microscopes (Titan Cubed 60-300 kV microscope (FEI) equipped with double Cs corrector from CEOS, and operated at 300 kV). Electron diffraction image was recorded using JEM 2010 transmission electron microscopes (JEOL). Strain analyses were based on GPA,³⁸ which was carried out using Gatan Digital Micrograph software.

Phase Field Simulation. The 3D phase-field models of the multilayer PTO/STO system were constructed. The order parameters were chosen as the three components of the polarization vectors. The system energy was composed of bulk, gradient, elastic, and electrostatic energies. The evolution of polarizations was simulated by the time-dependent Ginzburg–Landau equation: $dP_i/dt = -L \cdot \delta F / \delta P_i$. The corresponding energy functional formulas have been described in many previous literatures.^{49,50} The simulation models were discretized as $512 \times 2 \times Nz$. Choosing $Ny = 2$ means all domain walls were parallel to the y -direction, which was exactly the situation that we observe from a TEM image. The x - and y -directions were in the periodic boundary condition and mixed boundary condition was applied in the z -axis. The bottom of the system is subject to a constant displacement due to the misfit strain from the substrate, while the top of the system is in a stress-free state. The Landau–Devonshire coefficients of PTO and STO are adopted from previous literatures.^{49,51} At the interface between PTO and STO, we assume these coefficients change linearly across a certain zone. For the purpose of simplicity, all other material parameters of the whole system are taken as those of PTO, including the elastic constants, the dielectric constants, and the electrostrictive coefficients.⁴⁹

■ ASSOCIATED CONTENT

● Supporting Information

The Supporting Information is available free of charge on the ACS Publications website at DOI: [10.1021/acs.nanolett.7b02615](https://doi.org/10.1021/acs.nanolett.7b02615).

Crystal structure of ferroelectric PTO; 2D flux-closure arrays in eight layered PTO/STO films with the thickness ratio of 1 and 0.5 for adjacent PTO layers; phase field simulation details (PDF)

■ AUTHOR INFORMATION

Corresponding Authors

*E-mail: ylzhu@imr.ac.cn.

*E-mail: xlma@imr.ac.cn.

ORCID

Yin-Lian Zhu: [0000-0002-0356-3306](https://orcid.org/0000-0002-0356-3306)

Author Contributions

Y.L. and Y.J.W. contributed equally to this work. X.L.M. and Y.L.Z. conceived the project of interfacial characterization in oxides by using aberration-corrected STEM. Y.L., Y.L.Z., and X.L.M. designed the experiments. Y.L. performed the thin-film growth and STEM observations. Y.J.W., C.H.L., and J.L. carried out phase-field modeling simulations. Y.L.T., S.L., and S.R.Z. participated in the thin-film growth and STEM imaging. All authors contributed to the discussions and manuscript preparation.

Notes

The authors declare no competing financial interest.

■ ACKNOWLEDGMENTS

This work is supported by the National Natural Science Foundation of China (No. 51571197, 51231007, 51501194, 51671194, 51401212, and 51521091), National Basic Research Program of China (2014CB921002), and the Key Research Program of Frontier Sciences CAS (QYZDJ-SSW-JSC010). Y.L.T. acknowledges the IMR SYNLT-S. Kê Research Fellowship and the Youth Innovation Promotion Association CAS (No. 2016177). J.L. acknowledges the support by National Key Research Program of China (2016YFA0201001) and National Natural Science Foundation of China (No. 11627801).

■ REFERENCES

- (1) Seidel, J.; Martin, L. W.; He, Q.; Zhan, Q.; Chu, Y. H.; Rother, A.; Hawkrigde, M. E.; Maksymovych, P.; Yu, P.; Gajek, M.; et al. *Nat. Mater.* **2009**, *8*, 229–234.
- (2) Guyonnet, J.; Gaponenko, I.; Gariglio, S.; Paruch, P. *Adv. Mater.* **2011**, *23*, 5377–5382.
- (3) Balke, N.; Winchester, B.; Ren, W.; Chu, Y. H.; Morozovska, A. N.; Eliseev, E. A.; Huijben, M.; Vasudevan, R. K.; Maksymovych, P.; Britson, J.; et al. *Nat. Phys.* **2011**, *8*, 81–88.
- (4) Xu, T.; Shimada, T.; Araki, Y.; Wang, J.; Kitamura, T. *Nano Lett.* **2016**, *16*, 454–458.
- (5) Seidel, J.; Vasudevan, R. K.; Valanoor, N. *Adv. Electron Mater.* **2016**, *2*, 1500292.
- (6) Wu, Z. X.; Curtin, W. A. *Nature* **2015**, *526*, 62–67.
- (7) Peters, J. J. P.; Apachitei, G.; Beanland, R.; Alexe, M.; Sanchez, A. M. *Nat. Commun.* **2016**, *7*, 13484.
- (8) Chae, S. C.; Lee, N.; Horibe, Y.; Tanimura, M.; Mori, S.; Gao, B.; Carr, S.; Cheong, S. W. *Phys. Rev. Lett.* **2012**, *108*, 167603.
- (9) Gruverman, A.; Wu, D.; Fan, H. J.; Vrejoiu, I.; Alexe, M.; Harrison, R. J.; Scott, J. F. *J. Phys.: Condens. Matter* **2008**, *20*, 342201.
- (10) Rodriguez, B. J.; Gao, X. S.; Liu, L. F.; Lee, W.; Naumov, I. I.; Bratkovsky, A. M.; Hesse, D.; Alexe, M. *Nano Lett.* **2009**, *9*, 1127–1131.
- (11) Balke, N.; Choudhury, S.; Jesse, S.; Huijben, M.; Chu, Y. H.; Baddorf, A. P.; Chen, L. Q.; Ramesh, R.; Kalinin, S. V. *Nat. Nanotechnol.* **2009**, *4*, 868–875.
- (12) Vasudevan, R. K.; Chen, Y. C.; Tai, H. H.; Balke, N.; Wu, P. P.; Bhattacharya, S.; Chen, L. Q.; Chu, Y. H.; Lin, I. N.; Kalinin, S. V.; et al. *ACS Nano* **2011**, *5*, 879–887.
- (13) McQuaid, R. G.; McGilly, L. J.; Sharma, P.; Gruverman, A.; Gregg, J. M. *Nat. Commun.* **2011**, *2*, 404.
- (14) Ivry, Y.; Chu, D. P.; Scott, J. F.; Durkan, C. *Phys. Rev. Lett.* **2010**, *104*, 207602.
- (15) Chang, L. W.; Nagarajan, V.; Scott, J. F.; Gregg, J. M. *Nano Lett.* **2013**, *13*, 2553–2557.
- (16) Slutsker, J.; Artemev, A.; Roytburd, A. *Phys. Rev. Lett.* **2008**, *100*, 087602.
- (17) Naumov, I.; Fu, H. X. *Phys. Rev. Lett.* **2007**, *98*, 077603.
- (18) Schilling, A.; Byrne, D.; Catalan, G.; Webber, K. G.; Genenko, Y. A.; Wu, G. S.; Scott, J. F.; Gregg, J. M. *Nano Lett.* **2009**, *9*, 3359–3364.
- (19) Ng, N.; Ahluwalia, R.; Srolovitz, D. J. *Acta Mater.* **2012**, *60*, 3632–3642.
- (20) Chae, S. C.; Horibe, Y.; Jeong, D. Y.; Rodan, S.; Lee, N.; Cheong, S. W. *Proc. Natl. Acad. Sci. U. S. A.* **2010**, *107*, 21366–21370.
- (21) Choi, T.; Horibe, Y.; Yi, H. T.; Choi, Y. J.; Wu, W. D.; Cheong, S. W. *Nat. Mater.* **2010**, *9*, 253–258.
- (22) Hong, Z. J.; Damodaran, A. R.; Xue, F.; Hsu, S. L.; Britson, J.; Yadav, A. K.; Nelson, C. T.; Wang, J. J.; Scott, J. F.; Martin, L. W.; et al. *Nano Lett.* **2017**, *17*, 2246–2252.
- (23) Naumov, I. I.; Bellaiche, L.; Fu, H. X. *Nature* **2004**, *432*, 737–740.
- (24) Fu, H.; Bellaiche, L. *Phys. Rev. Lett.* **2003**, *91*, 257601.
- (25) McGilly, L. J.; Gregg, J. M. *Nano Lett.* **2011**, *11*, 4490–4495.

- (26) Nellist, P. D.; Chisholm, M. F.; Dellby, N.; Krivanek, O. L.; Murfitt, M. F.; Szilagy, Z. S.; Lupini, A. R.; Borisevich, A.; Sides, W. H.; Pennycook, S. J. *Science* **2004**, *305*, 1741–1741.
- (27) Mundy, J. A.; Brooks, C. M.; Holtz, M. E.; Moyer, J. A.; Das, H.; Rebola, A. F.; Heron, J. T.; Clarkson, J. D.; Disseler, S. M.; Liu, Z. Q.; et al. *Nature* **2016**, *537*, 523–527.
- (28) Nelson, C. T.; Winchester, B.; Zhang, Y.; Kim, S. J.; Melville, A.; Adamo, C.; Folkman, C. M.; Baek, S. H.; Eom, C. B.; Schlom, D. G.; et al. *Nano Lett.* **2011**, *11*, 828–834.
- (29) Jia, C. L.; Urban, K. W.; Alexe, M.; Hesse, D.; Vrejoiu, I. *Science* **2011**, *331*, 1420–1423.
- (30) Tang, Y. L.; Zhu, Y. L.; Ma, X. L.; Borisevich, A. Y.; Morozovska, A. N.; Eliseev, E. A.; Wang, W. Y.; Wang, Y. J.; Xu, Y. B.; Zhang, Z. D.; et al. *Science* **2015**, *348*, 547–551.
- (31) Tang, Y. L.; Zhu, Y. L.; Hong, Z. J.; Eliseev, E. A.; Morozovska, A. N.; Wang, Y. J.; Liu, Y.; Xu, Y. B.; Wu, B.; Chen, L. Q.; et al. *J. Mater. Res.* **2017**, *160*, 57–63.
- (32) Yadav, A. K.; Nelson, C. T.; Hsu, S. L.; Hong, Z.; Clarkson, J. D.; Schlepuetz, C. M.; Damodaran, A. R.; Shafer, P.; Arenholz, E.; Dedon, L. R.; et al. *Nature* **2016**, *530*, 198–201.
- (33) Evans, P. R.; Zhu, X. H.; Baxter, P.; McMillen, M.; McPhillips, J.; Morrison, F. D.; Scott, J. F.; Pollard, R. J.; Bowman, R. M.; Gregg, J. M. *Nano Lett.* **2007**, *7*, 1134–1137.
- (34) Scott, J. F. *Science* **2007**, *315*, 954–959.
- (35) Glazer, A. M.; Mabud, S. A. *Acta Crystallogr., Sect. B: Struct. Crystallogr. Cryst. Chem.* **1978**, *34*, 1065–1070.
- (36) Cohen, R. E. *Nature* **1992**, *358*, 136–138.
- (37) Catalan, G.; Seidel, J.; Ramesh, R.; Scott, J. F. *Rev. Mod. Phys.* **2012**, *84*, 119–156.
- (38) Hytch, M. J.; Snoeck, E.; Kilaas, R. *Ultramicroscopy* **1998**, *74*, 131–146.
- (39) Hytch, M. J.; Putaux, J. L.; Thibault, J. *Philos. Mag.* **2006**, *86*, 4641–4656.
- (40) Hytch, M. J.; Putaux, J. L.; Penisson, J. M. *Nature* **2003**, *423*, 270–273.
- (41) Meyer, B.; Vanderbilt, D. *Phys. Rev. B: Condens. Matter Mater. Phys.* **2002**, *65*, 104111.
- (42) Liu, Y.; Tang, Y. L.; Zhu, Y. L.; Wang, W. Y.; Ma, X. L. *Adv. Mater. Interfaces* **2016**, *3*, 1600342.
- (43) Tang, Y. L.; Zhu, Y. L.; Ma, X. L. *Ultramicroscopy* **2016**, *160*, 57–63.
- (44) Jia, C. L.; Mi, S. B.; Urban, K.; Vrejoiu, I.; Alexe, M.; Hesse, D. *Nat. Mater.* **2008**, *7*, 57–61.
- (45) Jia, C. L.; Nagarajan, V.; He, J. Q.; Houben, L.; Zhao, T.; Ramesh, R.; Urban, K.; Waser, R. *Nat. Mater.* **2007**, *6*, 64–69.
- (46) Liu, Y.; Zhu, Y. L.; Tang, Y. L.; Ma, X. L. *J. Mater. Res.* **2017**, *32*, 947–956.
- (47) Choi, K. J.; Biegalski, M.; Li, Y. L.; Sharan, A.; Schubert, J.; Uecker, R.; Reiche, P.; Chen, Y. B.; Pan, X. Q.; Gopalan, V.; Chen, L.-Q.; Schlom, D. G.; Eom, C. B. *Science* **2004**, *306*, 1005–1009.
- (48) Schlom, D. G.; Chen, L.-Q.; Eom, C.-B.; Rabe, K. M.; Streiffer, S. K.; Triscone, J.-M. *Annu. Rev. Mater. Res.* **2007**, *37*, 589–626.
- (49) Li, Y.; Hu, S.; Liu, Z.; Chen, L. *Acta Mater.* **2002**, *50*, 395–411.
- (50) Chen, L. Q. *J. Am. Ceram. Soc.* **2008**, *91*, 1835–1844.
- (51) Li, Y. L.; Hu, S. Y.; Tenne, D.; Soukiassian, A.; Schlom, D. G.; Xi, X. X.; Choi, K. J.; Eom, C. B.; Saxena, A.; Lookman, T.; et al. *Appl. Phys. Lett.* **2007**, *91*, 112914.